

Time- and frequency-domain subspace identification of a nonlinear spacecraft

J.P. Noël ¹, S. Marchesiello ², G. Kerschen ¹

¹ Space Structures and Systems Lab, Dept. of Aerospace and Mechanical Engineering, University of Liège
Chemin des chevreuils, 1 (B52/3), 4000 Liège, Belgium
e-mail: jp.noel@ulg.ac.be, g.kerschen@ulg.ac.be

² Dipartimento di Ingegneria Meccanica e Aerospaziale, Politecnico di Torino
Corso Duca degli Abruzzi, 24, 10129 Torino, Italy
e-mail: stefano.marchesiello@polito.it

Abstract

The present paper discusses the identification of the SmallSat spacecraft, a real-life nonlinear space structure developed by EADS-Astrium. To this end, two nonlinear subspace identification techniques formulated in the time and frequency domains are exploited, referred to as the TNSI and FNSI methods, respectively. The frequency response functions (FRFs) of the underlying linear spacecraft and the nonlinear coefficients are estimated by these approaches. The nonlinear component comprises an inertia wheel mounted on a support, the motion of which is constrained by eight elastomer plots and mechanical stops. This application is challenging for several reasons, which include high modal density, the discontinuous nature of the nonlinearities and order selection of the identified reduced model.

1 Introduction

Subspace techniques are powerful methods for identifying linear time-invariant systems. Several different formulations were proposed in the technical literature, both in the time [1] and frequency [2] domains. Nonlinear system identification is much more challenging, in particular in structural dynamics [3]. However, recent advances have shown that subspace-based algorithms can also be generalised to handle nonlinear systems of feedback form [4]. In particular, the Time- and Frequency-domain Nonlinear Subspace Identification (TNSI and FNSI) methods [5, 6] have proved to be effective for nonlinear system identification.

The present paper discusses the identification of the SmallSat spacecraft, a real-life nonlinear space structure developed by EADS-Astrium, using the TNSI and FNSI methods. The frequency response functions (FRFs) of the underlying linear spacecraft and the nonlinear coefficients are estimated by these approaches. The nonlinear component comprises an inertia wheel mounted on a support, the motion of which is constrained by eight elastomer plots and mechanical stops. This application is challenging for several reasons, which include high modal density, the discontinuous nature of the nonlinearities and order selection of the identified reduced model. In addition, this paper compares the accuracy and computational efficiency of the two methods. Their capability to retrieve the exact system order is also studied. The paper is organised as follows. Section 2 introduces the SmallSat structure and its finite element modelling. An overview of the TNSI and FNSI methods is given in Section 3 and their application to the SmallSat identification is carried out in Section 4. The conclusions of this application are summarised in Section 5.

2 The SmallSat spacecraft and its finite element modelling

The SmallSat structure has been conceived as a low-cost structure for small low-earth orbit satellite [7]. It is a monocoque tube structure which is 1.2 *m* long and 1 *m* large. It incorporates 8 flat faces for equipment mounting purposes, creating an octagon shape, as shown in Figure 1. The octagon is manufactured using carbon fibre reinforced plastic by means of a filament winding process. The structure thickness is 4.0 *mm* with an additional 0.25 *mm* thick skin of Kevlar applied to both the inside and outside surfaces to provide protection against debris. The interface between the spacecraft and launch vehicle is achieved through 4 aluminium brackets located around cut-outs at the base of the structure. The total mass including the interface brackets is around 64 *kg*. A finite element model (FEM) of the SmallSat was created in Samcef software and is used in the present study to conduct numerical experiments (Figure 2 (b)). It comprises about 65,000 degrees of freedom (DOFs) and the comparison with experimental measurements revealed its good predictive capability. The model idealises the composite tube structure using orthotropic shell elements and meets boundary conditions through 4 clamped nodes.



Figure 1: Picture of the SmallSat spacecraft and of the real WEMS device.

The SmallSat structure supports a telescope dummy composed of two stages of base-plates and struts supporting various concentrated masses; its mass is around 140 *kg*. The telescope dummy plate is connected to the SmallSat top floor via three shock attenuators, termed SASSA (Shock Attenuation System for Spacecraft and Adaptator) [8], the behaviour of which is considered as linear in the present study. The top floor is a 1 square meter sandwich aluminium panel, with 25 *mm* core and 1 *mm* skins, modelled using isotropic shell elements. Finally, as shown in Figure 2 (c), a support bracket connects to one of the 8 walls the so-called Wheel Elastomer Mounting System (WEMS) device which is loaded with an 8 *kg* inertia wheel dummy. The purpose of this device is to isolate the spacecraft structure from disturbances coming from the inertia wheel through the presence of a soft interface (made up of elastomer plots) between the fixed and mobile parts. In addition, mechanical stops limit the axial and lateral motion of the WEMS mobile part during launch, which gives rise to nonlinear dynamic phenomena. Figure 2 (d) depicts a simplified description of the overall device where the inertia wheel is considered to be a point mass. Shells model both the bracket and the wheel

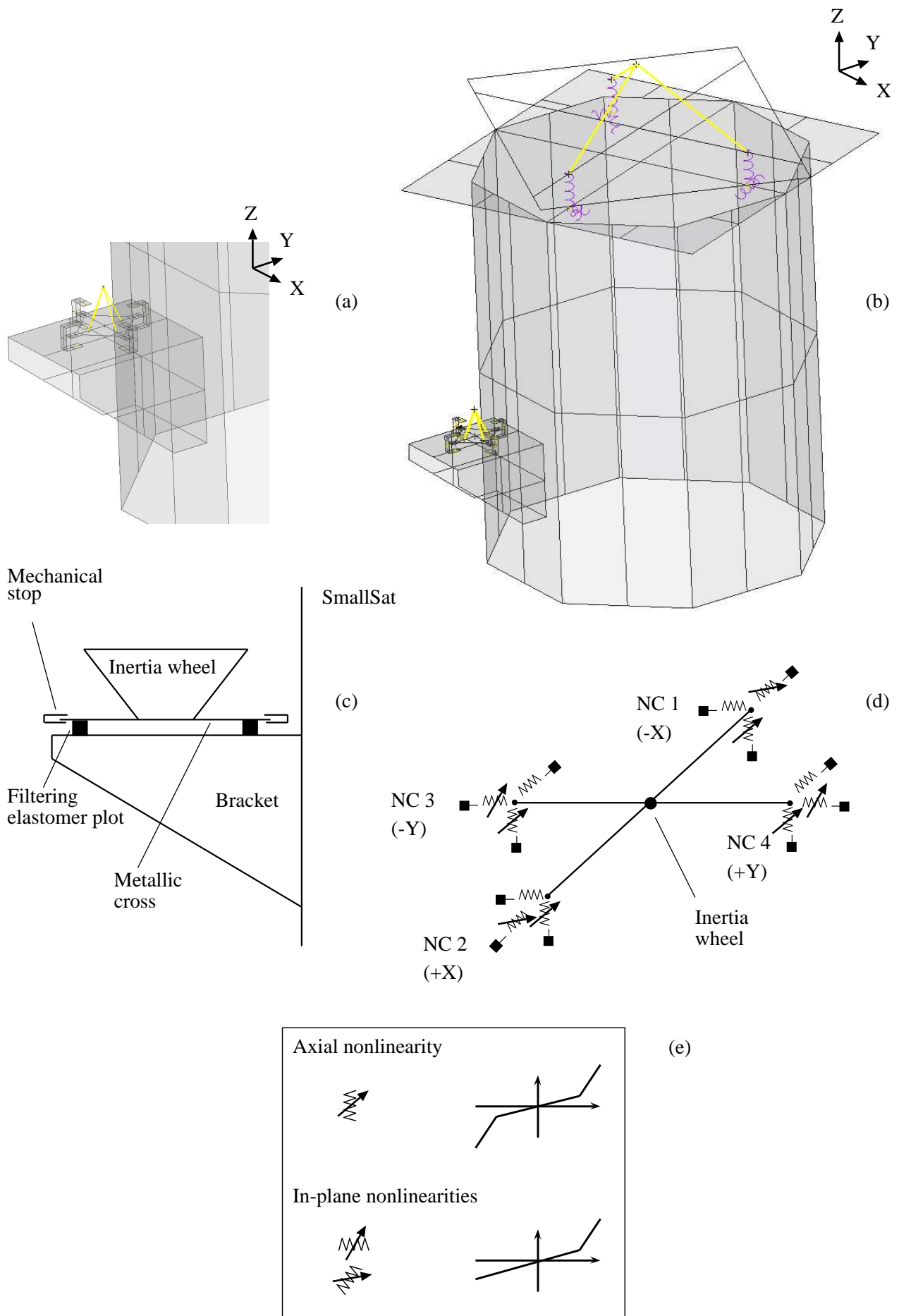


Figure 2: SmallSat FEM. (a) Zoom of the WEMS device; (b) global view; (c) detailed description of the WEMS components; (d) modelling of the WEMS mobile part; (e) close-up on the nonlinear restoring forces.

support (Figure 2 (a)). The four nonlinear connections between the WEMS mobile part (the inertia wheel and its cross-shaped support) and fixed part (the bracket and, by extension, the spacecraft itself) are labelled NC 1 – 4 and signalled through black squares. Each nonlinear connection possesses

- a nonlinear spring (elastomer in traction plus 2 stops) in the axial direction,
- a nonlinear spring (elastomer in shear plus 1 stop) in the radial direction,
- a linear spring (elastomer in shear) in the third direction.

The spring characteristics are piecewise linear and therefore non-regular at clearance. To avoid numerical issues, Hermite polynomials are implemented in the neighbourhood of the discontinuities to ensure C^1 continuity. The parameters of the WEMS stiffness curves are listed in Table 1, considering adimensional values for confidentiality reasons. The modelling includes bilateral nonlinearities in the axial direction and unilateral nonlinearities in the radial direction (Figure 2 (e)). Stops +X and +Y (resp. -X and -Y) can indeed only be impacted in positive (resp. negative) relative displacement.

	Clearance	Linear slope	Nonlinear slope
Axial Z	1	7.58	100
Lateral X and Y	1.29	1.97	39.7

Table 1: Adimensionalised parameters of the WEMS stiffness curves.

Global and local dissipation mechanisms are introduced in the FEM. A damping ratio of about 2 % is allocated to the spacecraft vibration modes below 100 Hz using the proportional damping rule $C = \alpha K + \beta M$ where C , K and M are the linear damping, stiffness and mass matrices, respectively. Acceptable parameters are $\alpha = 15.7 \cdot 10^{-5}$ and $\beta = 1.98$. Local dampers are then included to model dissipation in the elastomer plots, resulting in a non-proportional damping model and complex-valued vibration modes. A periodic noise forcing [9] with root-mean-square value of 200 N is applied to the inertia wheel node in the symmetric X – Y direction. It consists of a single band-limited (5 – 50 Hz) normally-distributed random signal (30,000 points, 12 seconds) repeated 8 times. This excitation causes the strong and comparable activation of all the WEMS nonlinearities, as confirmed in Table 2, which reports the number of clearance exceedances in the 8 nonlinear springs.

A nonlinear Newmark time integration scheme is used to conduct numerical experiments with a sampling frequency of 2,500 Hz. More precisely, because shocks on the metallic stops involve high-frequency oscillations, the sampling frequency is increased up to 20,000 Hz during integration prior to decimating the time series down to 2,500 Hz. The decimation process includes low-pass filtering to avoid aliasing.

	NC 1	NC 2	NC 3	NC 4
X	14,799	13,598	—	—
Y	—	—	13,476	13,020
Z	31,684	25,850	27,989	21,204

Table 2: Number of clearance exceedances. No entry means the absence of mechanical stop.

2.1 Linear modal analysis and reduced-order model

The 0 – 100 Hz frequency band comprises 18 linear normal modes (LNMs) of the structure. In particular, the WEMS local modes of vibration, likely to involve nonlinear dynamics, are located around 10 and 30 Hz. The interval between 50 and 100 Hz contains top plate modes involving SASSA deformations and global

modes of the structure. For nonlinear system identification purposes, we therefore limit our frequency range of interest to the 0 – 50 Hz interval or to the first 11 LNMs. Table 3 lists their natural frequencies ω together with a description of their deformed shapes.

Mode	Natural frequency ω (Hz)	Deformed shape
1	10.67	Local WEMS motion with concave trajectory along Y and small bracket bending about X
2	11.01	Local WEMS motion with concave trajectory along X and small bracket bending about Z
3	28.26	Local WEMS motion with convex trajectory along Y and small bracket bending about X
4	28.41	Local WEMS motion with convex trajectory along X and small bracket bending about Z
5	30.11	WEMS vertical motion and bracket bending about X
6	30.52	Local WEMS motion with rotation about Z and in-plane stretching
7	31.59	Top plate mode involving SASSAs in compression and small WEMS vertical motion
8	32.62	Top plate mode involving SASSAs in compression, main structure bending and WEMS vertical motion
9	37.42	Top plate mode involving SASSAs in shear
10	38.26	Top plate mode involving SASSAs in compression and shear and main structure bending
11	43.30	Top plate mode involving SASSAs in compression and shear

Table 3: Frequencies and deformed shapes of the first 11 LNMs of the SmallSat spacecraft.

For numerical investigations, a reduced-order model is created using the Craig-Bampton technique [10]. The method consists in describing the system in terms of some retained DOFs and internal vibration modes. 13 nodes (excluding DOFs in rotation) and 100 elastic modes (up to 444 Hz) are included in the condensed model, and reduced mass and stiffness matrices therefore share 139×139 dimensions. This reduced model is proved to accurately predict frequencies and LNMs up to 250 Hz , hence encompassing the seventh harmonics of the WEMS local modes. The first 4 retained nodes are located on the 4 ends of the metallic cross supporting the inertia wheel, and nodes 5 to 8 are taken on the bracket, respectively facing nodes 1 to 4. They are sorted according to the NC numbering introduced in Figure 2 (d). The inertia wheel point mass is the ninth retained node to which the excitation is applied. Finally, 4 nodes (numbered 10 to 13) positioned at the 4 top plate corners are included because they describe the deformed shape of several modes in the 0 – 50 Hz band.

3 Time- and frequency-domain nonlinear subspace identification

3.1 Problem statement

The classical identification process for nonlinear mechanical systems, described in [3], encapsulates three successive steps, namely detection, characterisation and parameter estimation. Once nonlinear behaviour is detected, a nonlinear system is said to be characterised after the location, type and functional form of all the nonlinearities throughout the system are determined. The parameters of the selected model are then estimated using linear least-squares fitting or nonlinear optimisation algorithms depending upon the method considered.

The TNSI and FNSI methods address this latter step and target the estimation of the nonlinear coefficients and FRFs of the underlying linear system. They assume that nonlinearities are localised and that there exists an underlying linear regime of vibration. The amplitude, the direction, the location and the frequency content of the excitation determine in which regime the structure behaves. The vibrations of such nonlinear systems are governed by the time-continuous model

$$M \ddot{q}(t) + C \dot{q}(t) + K q(t) + f(q(t), \dot{q}(t)) = p(t) \quad (1)$$

where $M, C, K \in \mathbb{R}^{r \times r}$ are the mass, damping and stiffness matrices, respectively; $q(t)$ and $p(t) \in \mathbb{R}^r$ are the generalised displacement and external force vectors, respectively; $f(t) \in \mathbb{R}^r$ is the nonlinear restoring force vector, and r is the number of DOFs of the structure obtained after spatial discretisation. As in reference [11], the effects of the s lumped nonlinearities are modelled using the summation

$$f(q(t), \dot{q}(t)) = \sum_{j=1}^s \mu_j b_j g_j(q(t), \dot{q}(t)). \quad (2)$$

Each term contains information about the unknown nonlinear coefficient μ_j and the corresponding functional form $g_j(t)$, which is assumed to be known. Nonlinearity location is specified using a vector of boolean values, $b_j \in \mathbb{R}^r$. In the literature about subspace methods, first-order state-space models are generally preferred to the second-order description of the dynamics in Equation (1), because the intrinsic capability of a state-space model to encompass multi-input, multi-output (MIMO) systems is attractive. Assuming that displacements are measured and defining the state vector $x = (q^T \ \dot{q}^T)^T \in \mathbb{R}^n$, the equations of motion are recast into

$$\begin{cases} \dot{x}(t) = A_c x(t) + B_c^{nl} g(t) + B_c p(t) \\ q(t) = C_c x(t) + D_c p(t) \end{cases} \quad (3)$$

where subscript c stands for *continuous-time*; $A_c \in \mathbb{R}^{n \times n}$, $B_c^{nl} \in \mathbb{R}^{n \times s}$, $B_c \in \mathbb{R}^{n \times r}$, $C_c \in \mathbb{R}^{r \times n}$ and $D_c \in \mathbb{R}^{r \times r}$ are the state, nonlinear coefficient, input, output and direct feedthrough matrices, respectively; $g(t) \in \mathbb{R}^s$ gathers the basis functions $g_j(t)$, and $n = 2r$. State-space and physical-space matrices correspond through the relations

$$A_c = \begin{pmatrix} 0^{r \times r} & \mathbf{I}^{r \times r} \\ -M^{-1} K & -M^{-1} C \end{pmatrix} \quad B_c^{nl} = \begin{pmatrix} 0^{r \times 1} & 0^{r \times 1} & \dots & 0^{r \times 1} \\ -\mu_1 M^{-1} b_1 & -\mu_2 M^{-1} b_2 & \dots & -\mu_s M^{-1} b_s \end{pmatrix}$$

$$B_c = \begin{pmatrix} 0^{r \times r} \\ M^{-1} \end{pmatrix} \quad C_c = \begin{pmatrix} \mathbf{I}^{r \times r} & 0^{r \times r} \end{pmatrix} \quad D_c = 0^{r \times r} \quad (4)$$

where 0 and I are zero and identity matrices, respectively. Given $p(t)$ and $q(t)$, the TNSI and FNSI methods determine the five matrices A_c , B_c^{nl} , B_c , C_c and D_c . The estimation of the nonlinear coefficients μ_j and FRFs is subsequently carried out thanks to the conversion from state space to physical space outlined in Section 3.5 and extensively discussed in [5].

3.2 Equivalent linear identification through feedback

The TNSI and FNSI methods utilise the feedback formulation proposed in [11], and illustrated in Figure 3, for interpreting the dynamics governed by Equation (1). It consists in moving the nonlinear term to the right-hand side of this equation and viewing nonlinear forces as external forces applied to the underlying linear structure. Thus, the internal forces that are nonlinear functions of the outputs act as a feedback to the linear open-loop system. Considering Equations (3), this interpretation boils down to the concatenation of $g(t)$ and $p(t)$ into a single *extended input* vector $e(t) \in \mathbb{R}^{s+r}$:

$$\begin{cases} \dot{x}(t) = A_c x(t) + B_c^e e(q(t), \dot{q}(t)) \\ q(t) = C_c x(t) + D_c^e e(t) \end{cases} \quad (5)$$

where $B_c^e = (B_c^{nl} \ B_c) \in \mathbb{R}^{n \times (s+r)}$ and $D_c^e = (0^{r \times s} \ D_c) \in \mathbb{R}^{r \times (s+r)}$.

The feedback formulation is particularly appealing, because the inverse problem to be solved is now equivalent to the widely-studied linear state-space identification problem. However, because the TNSI and FNSI algorithms handle nonlinearities in input-output (I-O) data, their interpretation and use must be tailored, as discussed throughout references [5, 6].

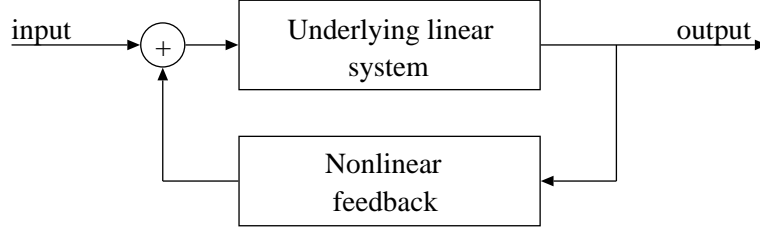


Figure 3: Feedback interpretation of nonlinear mechanical systems [11].

One remarks that, in practice, only a limited set of DOFs in $p(t)$ and $q(t)$ are excited and observed, respectively. The identification problem is therefore preferably stated in terms of the *measured* applied forces $u(t) \in \mathbb{R}^{m \leq r}$ and displacements $y(t) \in \mathbb{R}^{l \leq r}$. Accordingly, the extended input vector is $e(t) \in \mathbb{R}^{\sigma=s+m}$. Equations (5) become

$$\begin{cases} \dot{x}(t) &= A_c x(t) + B_c^e e(y(t), \dot{y}(t)) \\ y(t) &= C_c x(t) + D_c^e e(t) \end{cases} \quad (6)$$

where matrices A_c , B_c^e , C_c and D_c^e are now a projection of the original matrices onto the observed and controlled DOFs. Finally, a discrete-time translation of Equations (6) is considered, in particular for improved numerical conditioning in the frequency domain [12, 13]:

$$\begin{cases} x(t+1) &= A_d x(t) + B_d^e e(t) \\ y(t) &= C_d x(t) + D_d^e e(t) \end{cases} \quad (7)$$

where subscript d stands for *discrete-time*. This latter subscript will be skipped afterwards, because no ambiguity is possible.

3.3 Output-state-input matrix equation formulation

The TNSI and FNSI techniques both rely on a matrix formulation of Equations (7) encompassing all available time and frequency information, respectively. In the time domain, measured responses are arranged into Hankel-type block matrices. The output block Hankel matrix is defined as

$$Y_\mu = \begin{pmatrix} y(0) & y(1) & \dots & y(M-1) \\ y(1) & y(2) & \dots & y(M) \\ y(2) & y(3) & \dots & y(M+1) \\ \vdots & & & \\ y(\mu-1) & y(\mu) & \dots & y(\mu+M-2) \end{pmatrix} \in \mathbb{R}^{l\mu \times M} \quad (8)$$

where μ is a user-defined index and M is typically chosen to use all given data samples. The extended input block Hankel matrix, with the same block dimensions as Y_μ , is similarly defined as

$$E_\mu = \begin{pmatrix} e(0) & e(1) & \dots & e(M-1) \\ e(1) & e(2) & \dots & e(M) \\ e(2) & e(3) & \dots & e(M+1) \\ \vdots & & & \\ e(\mu-1) & e(\mu) & \dots & e(\mu+M-2) \end{pmatrix} \in \mathbb{R}^{\sigma\mu \times M}. \quad (9)$$

Introducing the extended observability matrix

$$\Gamma_\mu = \left(C^T \quad CA^T \quad CA^{2T} \quad \dots \quad CA^{\mu-2T} \quad CA^{\mu-1T} \right)^T \in \mathbb{R}^{l\mu \times n} \quad (10)$$

and the lower-block triangular Toeplitz matrix H_μ

$$H_\mu = \begin{pmatrix} D^e & 0 & 0 & \dots & 0 \\ CB^e & D^e & 0 & \dots & 0 \\ CAB^e & CB^e & D^e & \dots & 0 \\ \vdots & \vdots & \vdots & \ddots & \vdots \\ CA^{\mu-2}B^e & CA^{\mu-3}B^e & CA^{\mu-4}B^e & \dots & D^e \end{pmatrix} \in \mathbb{R}^{l\mu \times \sigma\mu}, \quad (11)$$

recursive application of Equations (7) results in the output-state-input matrix formulation

$$Y_\mu = \Gamma_\mu x + H_\mu E_\mu \quad (12)$$

where $x \in \mathbb{R}^{n \times M}$ is the state sequence, and the index μ is explicitly written to signal the number of block rows of a matrix.

In the frequency domain, the discrete Fourier transform (DFT) is first applied to Equations (7). Provided that the time signal $v(t)$ is periodic and observed over an integer number of periods in steady-state conditions, its DFT $V(k)$ is given by

$$V(k) = \frac{1}{\sqrt{M}} \sum_{t=0}^{M-1} v(t) e^{-j 2\pi k t/M} \quad (13)$$

where k is the frequency line and j the imaginary unit. Equations (7) thus write

$$\begin{cases} z_k X(k) = A X(k) + B^e E(k) \\ Y(k) = C X(k) + D^e E(k) \end{cases} \quad (14)$$

where $z_k = e^{j 2\pi k/M}$ is the Z-transform variable, and $X(k)$, $E(k)$ and $Y(k)$ are the DFTs of $x(t)$, $e(t)$ and $y(t)$, respectively. The output frequency spectra matrix is given by

$$Y_\nu = \begin{pmatrix} Y(1) & Y(2) & \dots & Y(N) \\ z_1 Y(1) & z_2 Y(2) & \dots & z_N Y(N) \\ z_1^2 Y(1) & z_2^2 Y(2) & \dots & z_N^2 Y(N) \\ \vdots & \vdots & \ddots & \vdots \\ z_1^{\nu-1} Y(1) & z_2^{\nu-1} Y(2) & \dots & z_N^{\nu-1} Y(N) \end{pmatrix} \in \mathbb{R}^{l\nu \times N} \quad (15)$$

where ν , similarly to μ , is a user-defined index and N the number of (non-necessarily equidistant) frequency lines exploited in the identification. Defining $\zeta = \text{diag}(z_1 \ z_2 \ \dots \ z_N) \in \mathbb{R}^{N \times N}$, Y_ν is recast into

$$Y_\nu = \left(Y^T \quad Y \zeta^T \quad Y \zeta^{2T} \quad \dots \quad Y \zeta^{\nu-1T} \right)^T. \quad (16)$$

The extended input frequency spectra matrix is accordingly formed as

$$E_\nu = \left(E^T \quad E \zeta^T \quad E \zeta^{2T} \quad \dots \quad E \zeta^{\nu-1T} \right)^T \in \mathbb{R}^{\sigma\nu \times N}. \quad (17)$$

Substitution of Equations (14) yields the mirror output-state-input matrix equation in the frequency domain

$$Y_\nu = \Gamma_\nu X + H_\nu E_\nu \quad (18)$$

where $X \in \mathbb{R}^{n \times N}$ is the state spectrum.

Remark that μ and ν must be chosen to encompass sufficient valuable information to identify the system, though a physics-based or information-based decision is delicate. Basically, the larger μ and ν , the more accurate the identification, because two indices convey how system dynamics is included in the data matrices. However, redundant information can affect the conditioning of those matrices, hence imposing bounds to μ and ν . There also exists an obvious trade-off between the values of μ , ν , M and N and the time needed to inverse the model. In particular, time-domain data are less compact than their frequency-domain counterpart, because one generally aims at building a model in a limited frequency band. In what follows, μ is chosen equal to 36 to avoid computational memory issues that can arise depending on the choice of M . In the case of FNSI, ν is set to 50.

3.4 Estimation of the state matrices

Nonlinear subspace identification algorithms are a three-step procedure built upon Equation (12) in the time domain and Equation (18) in the frequency domain. First, an estimate of the extended observability matrix Γ is computed (note that the indices μ and ν are dropped since the discussion is valid in the two domains). To this end, the terms depending on the input and the nonlinearities in Equations (12) and (18), namely $H_\mu E_\mu$ and $H_\nu E_\nu$, respectively, are eliminated using a geometrical projection. For instance in the frequency domain, Equation (18) is geometrically interpreted as the vector sum represented in Figure 4, in a two-dimensional space. An orthogonal projection onto the orthogonal complement of E_ν , denoted E_ν^\perp , cancels the extended input term.

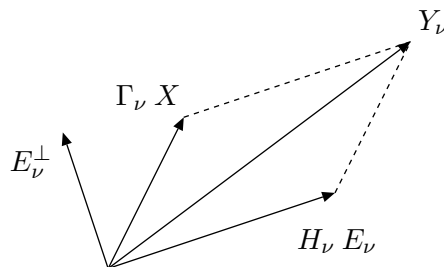


Figure 4: Geometrical interpretation of Equation (18) in a two-dimensional space.

Matrix Γ can then be obtained through a truncated singular value decomposition (SVD) of the result of the projection. The truncation limits the singular value spectrum to genuine elements, hence removing spurious values and reducing the influence of noise and rounding errors on the identification. In addition, the number of retained singular values yields the system order n . From the knowledge of n and Γ , the second step consists in computing the matrices A and C thanks to the shift property $\underline{\Gamma} A = \overline{\Gamma}$, where $\underline{\Gamma}$ and $\overline{\Gamma}$ are the matrix Γ without the last and first l rows (or block row), respectively. State matrix A is thus found as the least-squares solution of the overdetermined system of equations $A = \underline{\Gamma}^\dagger \overline{\Gamma}$, where \dagger is the pseudo-inverse; output matrix C is extracted from Γ as its l first rows. The final step is the estimation of the system matrices B^e and D^e . Two robust numerical schemes are described in references [1] and [6] for the time- and frequency-domain resolutions, respectively. They exploit the formulation of a set of linear equations in B^e and D^e , explicitly solved in least-squares sense. For the sake of conciseness, they are not detailed herein.

3.5 Conversion from state space to physical space

Starting from the identified spate-space model (A, B^e, C, D^e) , the estimation of the nonlinear coefficients μ_j and the FRFs of the underlying linear system $H(\omega)$ can be carried out. To this end, a transformation back to

physical space is achieved through the derivation of a linear relationship between output and extended input spectra in lumped nonlinear structures, extending the concept of FRF [11]:

$$Y(\omega) = H(\omega) \left[\mathbf{I}^{r \times r} - \sum_{j=1}^s \mu_j b_j \right] E(\omega) = H^e(\omega) E(\omega) \quad (19)$$

where the linear operator $H^e(\omega)$ is the extended FRF matrix. Moreover, reference [5] proves that $H^e(\omega)$ is an invariant system property. It can be retrieved, as in linear theory, from the combination of the continuous-time state-space matrices

$$H^e(\omega) = C_c(j\omega \mathbf{I}^{n \times n} - A_c)^{-1} B_c^e + D_c^e. \quad (20)$$

As a result, the nonlinear coefficients identified from the extended FRF matrix are complex-valued and frequency-dependent. A reliable identification scheme together with an appropriate selection of the nonlinear functional forms should make the imaginary parts much smaller than the corresponding real parts. The frequency dependence of the coefficients should also remain small. These indications will serve as quality criteria in Section 4.

4 Identification of the SmallSat spacecraft

This section addresses the identification of the SmallSat structure using the TNSI and FNSI methods. First, the transients in the system response are inspected in order to select the data samples processed by the two methods. Second, the problem of determining the order of the identified model is carefully analysed using two decision-making tools, namely the singular value plot (SVP) and the stabilisation diagram. The TNSI and FNSI estimations of the underlying linear and nonlinear parameters of the system are then commented and compared. Finally, the reduction of modelling errors in the frequency domain is discussed.

4.1 Transient analysis

References [9, 14] recommend to carry out a transient analysis prior to starting the identification process. A simple means of revealing transients (and leakage in the frequency domain) is to make explicit use of the periodicity of the excitation. To this end, 4 periods of the displacement of the inertia wheel measured in the direction of excitation are plotted in Figure 5 (a), where deviations from periodicity are hardly detectable. Transients can be made visible by subtracting the fourth period from the signal, as shown in Figures 5 (b) and (c). From the logarithmic plot in Figure 5 (c), the transient is found to decay exponentially and to die out after two periods. In the frequency domain, the analysis of the DFT of the response over successive periods, as represented in Figures 5 (d) to (f), also proves that the system reaches steady-state oscillations from the third recorded period.

In the application of the TNSI method, the transient response is found to yield improved results compared with the steady-state regime, in particular in the estimation of the linear modal properties. The first 30,000 recorded samples (or first period) will therefore be considered in the time-domain identification. For the FNSI method, 180,000 time samples (or 6 periods) are retained after the rejection of the 2 first periods of measurement to avoid leakage. After applying the DFT, only 3,240 frequency lines spanning from 5 to 50 Hz will finally be exploited in the inverse problem. In this application, 9 inputs, namely the external forcing and the 8 nonlinearities, and 18 outputs are considered. The outputs include the 16 nonlinear channels and the displacements of the inertia wheel in the axial and excitation directions.

4.2 Estimation of the linear and nonlinear parameters

The first step in formulating a nonlinear subspace-based model is the selection of the model order. This step is crucial since too low orders involve unmodeled dynamics whereas too large orders increase the noise

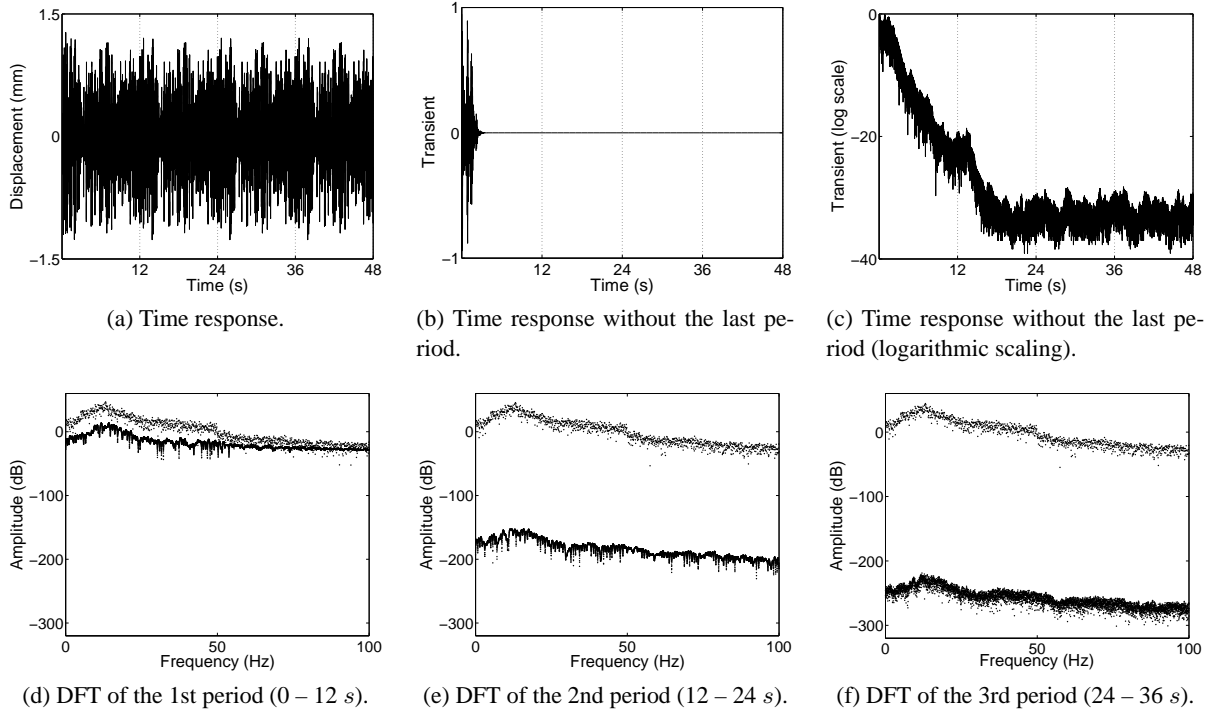


Figure 5: Transient analysis of the system output. The periodicity of the excitation is explicitly exploited in the time domain (a-c). The DFT of the response also reveals transients in the frequency domain (d-f).

sensitivity of the model [9]. A basic decision-making tool in subspace applications is a SVP, depicted in Figures 6 (a) and (b) for the time- and frequency-domain methods, respectively. For TNSI, several jumps in magnitude are observed and about 30 singular values can be differentiated from the continuum of spurious elements. This high number of eligible modes is due to the processing of the full frequency content of the measurements in the time domain. We opt for the order 16 because it corresponds to the larger jump, although a number of significant values and jumps exists in the diagram. An increase of the number of block rows μ would probably enhance the readability of this latter diagram, but is not within reach because of computational memory constraints. For FNSI, the restriction of the spectra into 5 – 50 Hz bounds the number of identifiable modes but facilitates the selection of the order, *i.e.*, 10.

In linear subspace identification, the SVP is always disregarded in favour of the stabilisation diagram [15]. Because the TNSI and FNSI algorithms succeed in decoupling linear parameters from nonlinear distortions, the use of stabilisation diagrams in nonlinear system identification is still effective. Figures 7 (a) and (b) depict the stabilisation of the natural frequencies, damping ratios and complex mode shapes for increasing model orders up to 60. The modal assurance criterion for complex-valued mode shapes (MACX), as defined in [16], is utilised in these two diagrams. Figure 7 (a) shows stabilisation defects at order 16 in disagreement with the jump in the SVP. One also remarks that, amongst the 8 retained modes, 3 of them are located outside the input band and weakly participate in the system dynamics. Figure 7 (b) indicates that the order 10 is adequate for FNSI even though stabilisation defects are also present in the diagram. Note that stabilisation is assessed between successive orders (say, n and $n + 2$) taking as reference the linear properties extracted at order n . This explains why the order 10 in Figure 7 (b) is apparently unstabilised though the frequency, damping ratio and MACX indicators at order 12 prove the opposite.

Table 4 lists the relative errors on the estimated natural frequencies and damping ratios together with the MACX values between the identified and exact complex mode shapes for the TNSI and FNSI methods, respectively. The two methods accurately recover the linear parameters of the structure in 0 – 50 Hz from strongly nonlinear measurements. This constitutes a major asset of the TNSI and FNSI methods, which

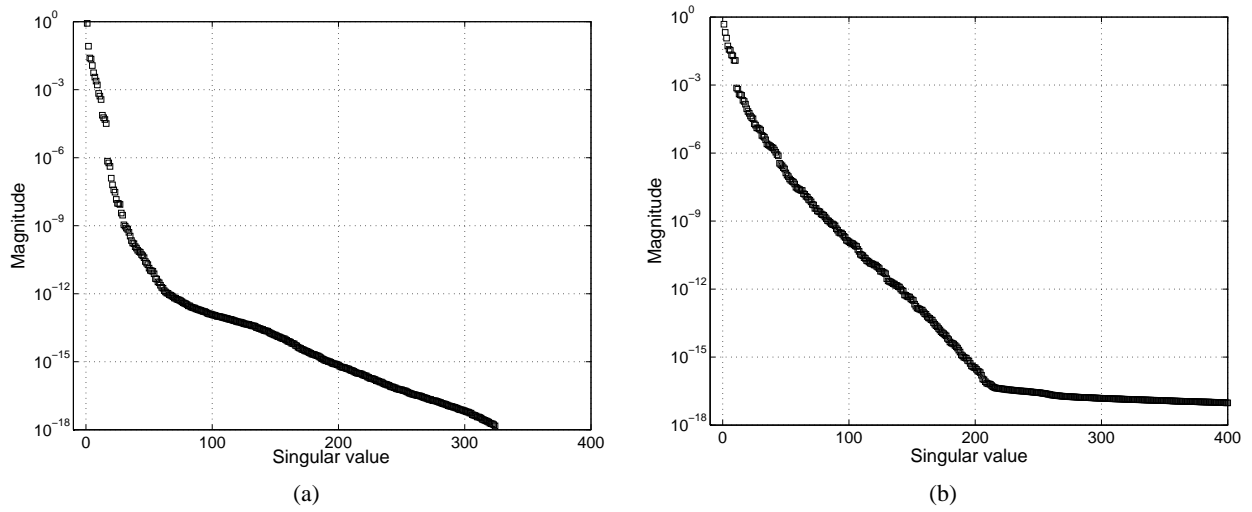


Figure 6: Singular values for (a) the TNSI and (b) FNSI methods.

however heavily depends on an appropriate choice of the nonlinear functional forms. It is also worth noticing that the linear parameters of the 3 out-of-input-band modes in Figure 7 (a) are less convincing. Note also that the somehow surprising MACX values for these 3 modes will be justified below.

The 8 nonlinear coefficients are shown in Figures 8 and 9, where the TNSI and FNSI results are depicted using solid and dashed lines, respectively. Numerical detail is given in Table 5 through averaged values, relative errors and ratios (in logarithmic scale) between real and corresponding imaginary parts. One limits the averaging interval to 40 Hz since the modes mainly governing the system response are located around 10 and 30 Hz. The quality of the identification is excellent for both subspace methods. The real parts generally remain bounded within a 10 %-interval around the exact values and the imaginary parts are at least 2 orders

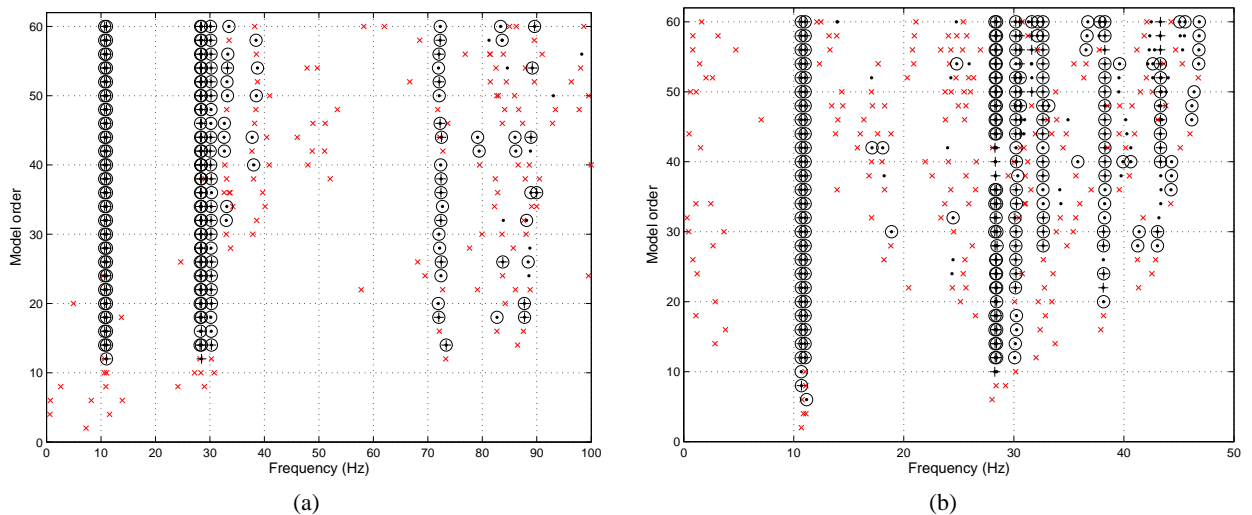


Figure 7: Stabilisation diagrams for (a) the TNSI and (b) FNSI methods. ●: stabilisation in natural frequency; + and ○: extra stabilisation in damping ratio and MACX value, respectively; ×: unstabilised pole. Stabilisation thresholds in natural frequency, damping ratio and MACX value are 0.5 %, 2 % and 0.98, respectively.

of magnitude lower.

A closer inspection of the FNSI coefficients reveals that they exhibit somewhat larger frequency variations than the TNSI estimates. This discrepancy is to be attributed to the reduced number of modes captured in the frequency-domain identification. In other words, linear modelling errors manifest themselves in the coefficients as a frequency dependence. Therefore, to reduce modelling errors, a second FNSI analysis can be carried out considering spectra from 5 to 100 Hz and selecting the order 16, similarly to TNSI. Figures 8 and 9 show the results using dotted lines. One observes that the accuracy reached by the two methods is now comparable, as confirmed by the numerical values reported in Table 5. The estimated natural frequencies, damping ratios and modes shapes are also found to be in close agreement with the exact values in Table 4. MACX matrices are finally displayed in Figures 10 (a) and (b) for the TNSI and FNSI methods at the same order, and show that the two methods suffer from the same inversion between the 7th and 8th identified modes.

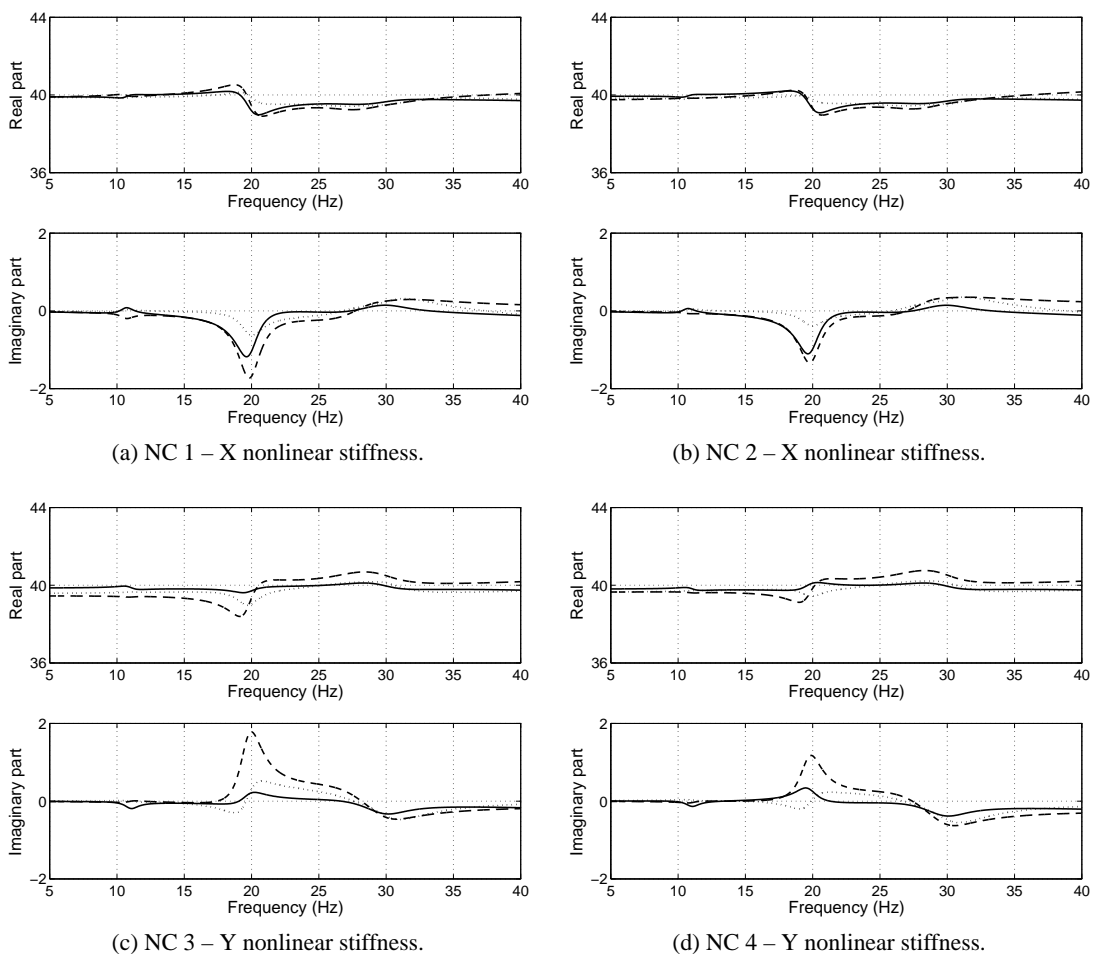


Figure 8: TNSI (solid line) and FNSI (dashed and dotted lines over 0 – 50 Hz and 0 – 100 Hz , respectively) estimations of the lateral nonlinear coefficients. The real parts are displayed within 10 %-error bounds.

5 Conclusions

This paper aimed at identifying the SmallSat spacecraft, a strongly nonlinear space structure developed by EADS-Astrium, from synthetic data. To this end, two nonlinear generalisations of subspace methods, namely TNSI and FNSI methods, were exploited. The nonlinear coefficients and the underlying linear parameters

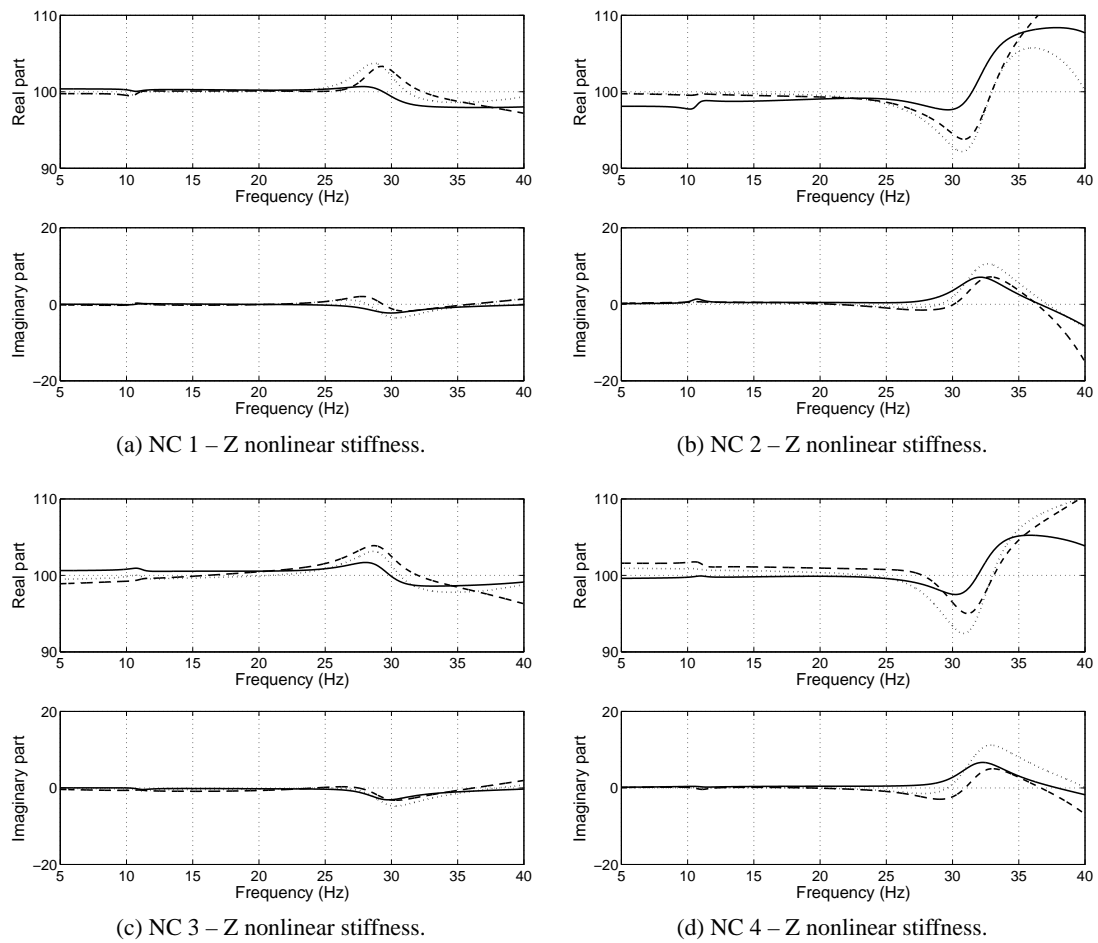


Figure 9: TNSI (solid line) and FNSI (dashed and dotted lines over 0 – 50 Hz and 0 – 100 Hz, respectively) estimations of the axial nonlinear coefficients. The real parts are displayed within 10 %-error bounds.

of the structure were accurately estimated and a comparison between the two methods in terms of efficiency was outlined. This study is arguably one of the first successful identification of such a complex nonlinear real-life structure in the technical literature.

However, additional investigations are needed to further assess the capabilities of the two techniques. The influence of noise on the identification results should be carefully analysed. The use of stabilisation diagrams in nonlinear system identification, initiated in the present paper, should also be studied in more detail.

Acknowledgements

This paper has been prepared in the framework of the ESA Technology Research Programme study "Advancement of Mechanical Verification Methods for Non-linear Spacecraft Structures (NOLISS)" (ESA contract No.21359/08/NL/SFe – Grant manager: A. Newerla).

The author J.P. Noël would like to acknowledge the Belgian National Fund for Scientific Research (FRIA fellowship) for its financial support.

Identified mode (exact ω in Hz)	Error on ω (%)			Error on ϵ (%)			MACX values		
	TNSI	FNSI		TNSI	FNSI		TNSI	FNSI	
		5 – 50 / 100 Hz			5 – 50 / 100 Hz			5 – 50 / 100 Hz	
1 (10.67)	0.08	0.19	0.19	-0.25	-0.35	-0.28	1.00	1.00	1.00
2 (11.01)	0.09	0.19	0.20	-0.01	-0.08	-0.13	1.00	1.00	1.00
3 (28.26)	-0.06	0.01	0.03	0.53	-1.70	-1.43	1.00	0.99	1.00
4 (28.41)	0.10	0.11	0.13	0.66	-0.02	0.46	1.00	1.00	1.00
5 (30.11)	0.44	0.18	0.38	8.89	6.02	7.80	1.00	1.00	1.00
6 (71.94)	0.22	—	-3.19	41.74	—	19.00	1.00	—	0.99
7 (80.48)	2.73	—	0.23	187.81	—	-46.87	0.00	—	0.00
8 (84.29)	3.88	—	-1.74	64.69	—	-59.17	0.00	—	0.00

Table 4: Relative errors between the estimated and exact natural frequencies ω and damping ratios ϵ ; MACX values between estimated and exact complex mode shapes. Left columns for TNSI and middle and right columns for FNSI over 5 – 50 Hz and 5 – 100 Hz , respectively.

Nonlinear coefficient	Averaged value			Error (%)			Ratio real/imag. (log scaling)		
	TNSI	FNSI		TNSI	FNSI		TNSI	FNSI	
		0 – 50 / 100 Hz			0 – 50 / 100 Hz			0 – 50 / 100 Hz	
NC 1 – X	39.75	39.77	39.76	0.13	0.18	0.14	2.53	2.49	3.24
NC 2 – X	39.79	39.73	39.73	0.22	0.08	0.09	2.56	3.00	3.18
NC 3 – Y	39.86	39.84	39.71	0.40	0.35	0.02	2.75	2.67	2.99
NC 4 – Y	39.87	40.00	39.80	0.43	0.75	0.24	2.73	3.12	2.68
NC 1 – Z	99.67	99.94	100.10	-0.33	-0.06	0.06	2.37	3.92	2.52
NC 2 – Z	100.58	100.76	99.55	0.58	0.76	-0.45	2.01	3.63	1.99
NC 3 – Z	100.19	100.00	99.75	0.19	-0.00	0.25	2.18	2.19	2.06
NC 4 – Z	100.60	101.54	100.90	0.60	1.54	0.90	1.95	2.78	1.81

Table 5: Estimated nonlinear parameters (real parts), relative errors and ratios (in logarithmic scale) between real and imaginary parts. Left columns for TNSI and middle and right columns for FNSI over 5 – 50 Hz and 5 – 100 Hz , respectively.

References

- [1] P. Van Overschee and B. De Moor. *Subspace Identification for Linear Systems*. Kluwer Academic Publishers, 1996.
- [2] T. McKelvey, H. Akçay, and L. Ljung. Subspace-based multivariable system identification from frequency response data. *IEEE Transactions on Automatic Control*, 41:960–979, 1996.
- [3] G. Kerschen, K. Worden, A. F. Vakakis, and J.C. Golinval. Past, present and future of nonlinear system identification in structural dynamics. *Mechanical Systems and Signal Processing*, 20:505–592, 2006.
- [4] S. L. Lacy and D. S. Bernstein. Subspace identification for non-linear systems with measured-input non-linearities. *International Journal of Control*, 78:906–926, 2005.
- [5] S. Marchesiello and L. Garibaldi. A time domain approach for identifying nonlinear vibrating structures by subspace methods. *Mechanical Systems and Signal Processing*, 22:81–101, 2008.
- [6] J.P. Noël and G. Kerschen. A new subspace-based approach to identify nonlinear mechanical structures in the frequency domain. In *16th IFAC Symposium on System Identification*, 2012.

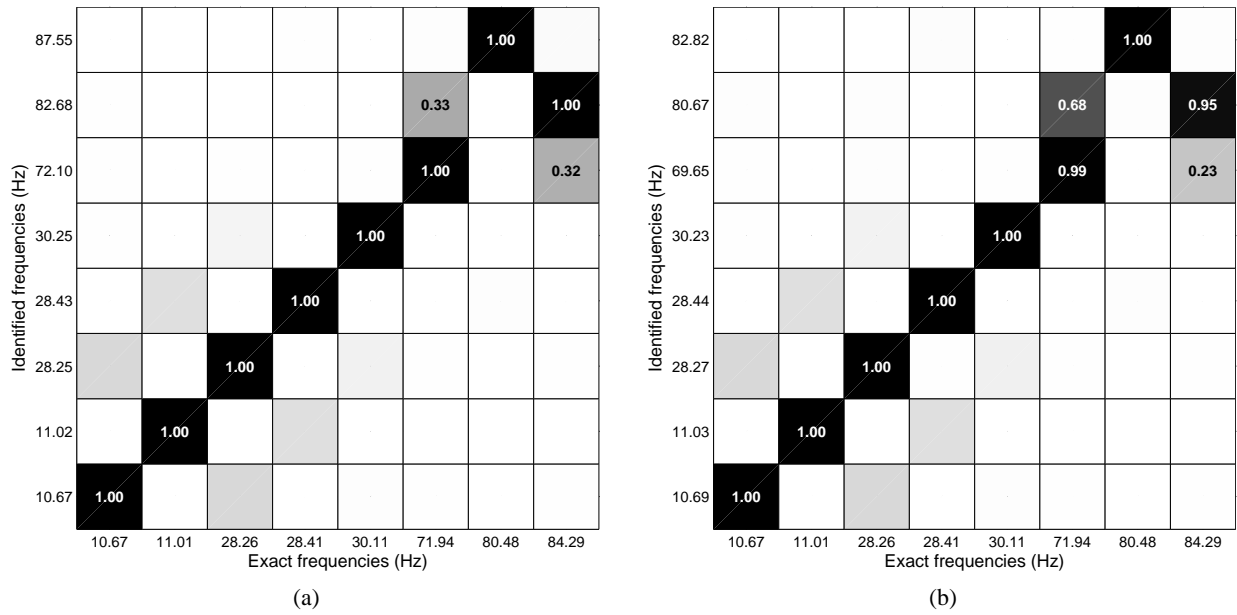


Figure 10: MACX matrices between the estimated and exact complex mode shapes for (a) the TNSI and (b) FNSI methods at order 16.

- [7] A. G. Russell. Thick skin, faceted, cfrp, monocoque tube structure for smallsats. In *European Conference on Spacecraft Structures, Materials and Mechanical Testing*, 2000.
- [8] P. Camarasa and S. Kiryenko. Shock attenuation system for spacecraft and adaptor (sassa). In *European Conference on Spacecraft Structures, Materials and Mechanical Testing*, 2009.
- [9] R. Pintelon and J. Schoukens. *System Identification: A Frequency Domain Approach*. IEEE Press, 2001.
- [10] R. Craig and M. Bampton. Coupling of substructures for dynamic analysis. *AIAA Journal*, 6:1313–1319, 1968.
- [11] D. E. Adams and R. J. Allemang. A new derivation of the frequency response function matrix for vibrating non-linear systems. *Journal of Sound and Vibration*, 227:1083–1108, 1999.
- [12] P. Van Overschee and B. De Moor. Continuous-time frequency domain subspace system identification. *Signal Processing*, 52:179–194, 1996.
- [13] Z. J. Yang and S. Sanada. Frequency domain subspace identification with the aid of the w-operator. *Electrical Engineering in Japan*, 132(1):46–56, 2000.
- [14] J. Schoukens, R. Pintelon, and Y. Rolain. *Mastering System Identification in 100 Exercises*. Wiley-IEEE Press, 2012.
- [15] E. Reynders and G. De Roeck. Reference-based combined deterministic-stochastic subspace identification for experimental and operational modal analysis. *Mechanical Systems and Signal Processing*, 22:617–637, 2008.
- [16] P. Vacher, B. Jacquier, and A. Bucharles. Extensions of the mac criterion to complex modes. In *ISMA 2010 International Conference on Noise and Vibration Engineering*, 2010.